Materials and Structures (2026) 59:274
https://doi.org/10.1617/s11527-026-03023-6

ORIGINAL ARTICLE

Experimental and numerical study on the inter-layer shear behavior of 3D printed concrete

Lucia Licciardello · Adriano Reggia · Giovanni Metelli · Giovanni A. Plizzari

Received: 22 October 2025 / Revised: 30 January 2026 / Accepted: 18 February 2026

Abstract 3D printing of concrete offers numerous advantages for the fabrication of architectural and structural components, such as cost-effectiveness, time savings, and enhanced quality. Although the potential of this technology has been widely demonstrated, it appears necessary to continue scientific research, as traditional testing methodologies for conventional concrete have been adapted to investigate phenomena of 3D printed concrete (3DPC) elements. This study aims to address this need by focusing on evaluating the inter-layer shear behavior of hardened 3DPC. A novel test method, adapted from masonry and concrete testing, was employed to conduct push-out tests on 3DPC specimens. The test set-up aims to induce shear forces along inter-layer surfaces under varying levels of normal compression (*i.e.*, confining stress). The experimental results allowed the assessment of the shear behavior of the inter-layer surface in terms of interface shear strength, shear stiffness, cohesion, and friction angle. Additionally, non-linear finite element analyses (NLFEA) were conducted and validated against experimental results, providing valuable/effective tools for structural modeling of 3DPC elements. Both smeared crack and discrete crack approaches to non-linear fracture mechanics demonstrated good agreement with experimental observations. The comparison was effective regarding pre-peak and post-peak behavior, interface shear strength, cohesion, and friction angle.

Keywords 3D Concrete Printing · Directionality · Push-out test · Numerical modeling

1 Introduction

3D printing of concrete is a modern digital fabrication method which can radically change the production of architectural and structural components in a few years. By integrating digital design and construction processes, 3D printing of concrete presents significant economic and environmental advantages, including reduced construction time, costs and better quality of members [1, 2]. Advancements in concrete properties and printing technologies have stimulated construction companies to embark on printing some prototype buildings. Two prominent approaches have emerged: on-site and off-site construction. On-site printing involves creating structures in an open environment, while off-site printing refers to the

L. Licciardello (✉) · A. Reggia · G. Metelli · G. A. Plizzari
Department of Civil, Environmental, Architectural Engineering and Mathematics, University of Brescia, Brescia, Italy
e-mail: l.licciardello@unibs.it

A. Reggia
e-mail: adriano.reggia@unibs.it

G. Metelli
e-mail: giovanni.metelli@unibs.it

G. A. Plizzari
e-mail: giovanni.plizzari@unibs.it

Published online: 16 June 2026

production of prefabricated elements in laboratory for subsequent on-site assembly, on the basis of a modular construction approach. Noteworthy projects using concrete extrusion for on-site printing include the Milan (Italy) prototype house (2018) [3], the Beckum (Germany) two-story residential building (2021) [4, 5], and the Wave House in Heidelberg (Germany) [6]. Off-site approach has been successfully used for the construction of small bridges, such as the bicycle bridge in Gemert (the Netherlands) [7], the pedestrian bridge in Nijmegen (the Netherlands) [8], and the Phoenix bridge in Lyon [9]. Further examples of off-site construction are the DFAB house (Dubendorf, Switzerland) [10–14] and the Tor Alva (Mulegns, Switzerland) [15, 16].

While these projects have demonstrated the technology potential to realize prototypes with varying shapes and geometries, scientific research work on the structural behavior of 3D printed concrete (3DPC) members is needed at both the micro and macro scales. An area of particular interest involves the comprehension of the structural effects related to the layered structure of 3DPC elements. Unlike traditional concrete structures, the presence of interfaces between subsequent printed layers can generate a potentially anisotropic behavior, thus affecting the shear and flexural bearing mechanisms of the structural elements. To this aim, it should be noted that many researchers are committed to the assessment of the properties of the printed material in both its fresh and hardened states [17–35], as these aspects can impact the overall structural performance of 3DPC elements.

In the fresh state, 3D printed materials behave as a visco-plastic material, especially during pumping and extrusion phases [17], whereas the shape of the deposited layer is governed by the elasto-plastic properties [17]. Due to the absence of traditional formwork, the mechanical properties of fresh concrete, such as the elastic modulus, the Poisson's ratio, the compressive strength, and their evolution over time, become crucial factors in managing the structural behavior during the fabrication process. The material properties can be evaluated through unconfined compression tests [18–20], shear tests [21, 22], and triaxial tests [21]. It is necessary to control pumpability (*i.e.*, the transport of fresh material from the pump to the extrusion nozzle [23]), extrudability (*i.e.*, the ability to extrude the material through the nozzle without significant cross-sectional deformation [23]), and buildability (*i.e.*, the ability to print a specific number of layers [23]) to prevent buckling and plastic collapse, which may be possible failure modes.

In the hardened state, extrusion-based 3D printed concrete exhibits an inherent mechanical anisotropy due to the layer-by-layer deposition and the presence of interlayer regions. Therefore, interfaces play an important role, as their strength is significantly affected by the direction of the applied load with respect to the printing direction [33]. This characteristic often makes traditional tests for conventional concrete inadequate, requiring them to be adapted for 3D printed concrete materials. Extensive research has been carried out on the determination of the compressive properties of 3DPC, which consisted of carrying out uniaxial compression tests on cubic or cylindrical specimens [24–31], similar to cast-in-place concrete. Regarding the tensile properties, the flexural tensile strength of concrete is commonly measured through a three-point bending test [24–32] and the tensile strength through pull-off tests [26, 29, 30, 32, 36]. To account for anisotropy induced by the printing process, as shown in recent studies [24–32], 3DPC specimens were tested with respect to three mutually orthogonal directions. It resulted that the direction of loading had little effect on the compressive properties, as the difference in compressive strength was less than 10%. However, the influence on flexural tensile strength was more pronounced since its variation ranged between 20 and 25%, depending on the loading direction. The highest flexural strength values were observed when the load was applied perpendicular to the layer interfaces.

Only a few studies can be found in the literature on the assessment of the interface strength of 3D printed concrete under shear loading. Napolitano et al. [37] proposed a specific test that induced the sliding fracture at the layer-to-layer interface of 3DPC specimens (Fig. 1a). This study aimed to investigate the strength at the interface without the application of confining stresses, focusing on different time intervals between the placement of successive layers, which significantly impacted the interface strength, leading to a substantial decrease in the maximum shear load as compared to cast concrete elements. This test was similar to the test on triplets of bricks used to assess the shear properties of masonry structures [38]. Alchaar et al. [39] investigated the effect of different

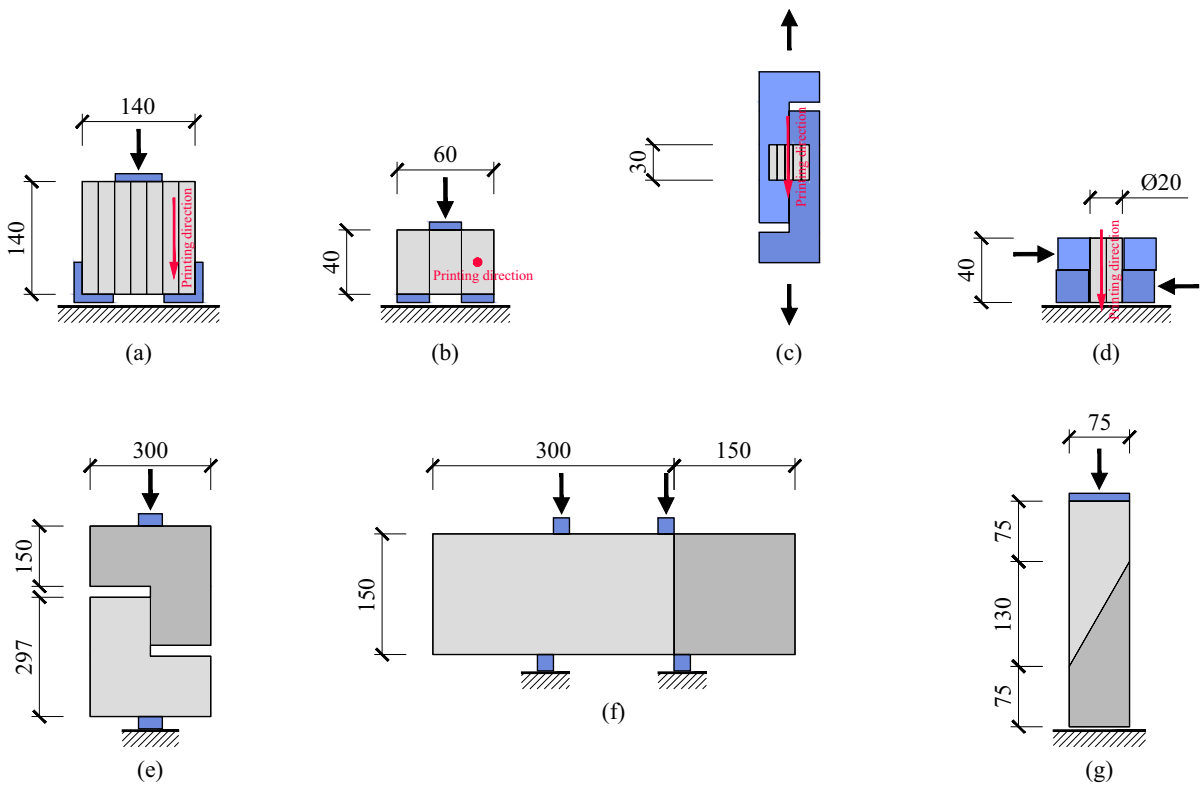

Fig. 1 Shear test examples for masonry and concrete: adapted from Napolitano et al. [37] (**a**), adapted from Alchaar et al. [39] (**b**), adapted from Rahul et al.[40], and Meurer et al. [41] (**c**), adapted from Van der Heever et al. [42] (**d**), adapted from Giraldo-Soto et al. [45] (**e**, **f**), and adapted from Zanotti et al. [46] (**g**)

printing time intervals and high temperatures on the shear strength of the interlayer in specimens without confining stress. The test setup involved loading the mid-layer of a specimen, consisting of three stacked layers, until failure (Fig. 1b). It was observed that the interface strength decreases with longer time intervals (between layers) and higher temperatures, due to accelerated moisture loss and faster surface dehydration. Rahul et al. [40] and Meurer et al. [41] also investigated the effect of time interval on the interface shear strength. The first [40] conducted direct shear tests on cylindrical specimens with a diameter of 25 mm and a height of 40 mm. A dedicated test setup was used to generate uniform interface shear stresses (Fig. 1c). The specimens were positioned horizontally in the grooves of the upper and lower jaws, with the interface located at mid-height. Relative to the corresponding mold-cast concrete, a reduction of the interlayer shear strength was observed. The second [41] proposed a specific shear test on small drill cores (29.5 mm diameter) extracted from printed elements to approximate a near-pure and uniform shear stress distribution while limiting size effects. The setup is conceptually similar to that shown in Fig. 1c; however, specimen rotation is restrained and only longitudinal sliding is permitted, minimizing unintended restraint forces at the interface. The authors expected the interlayer shear strength to decrease with increasing interval time, consistent with the trends of tensile and flexural strength. However, the assessment of the influence of the interval time remained inconclusive. This was mainly due to the concrete mixing procedure, which required the addition of fresh concrete during printing, increasing the interface moisture and artificially enhancing the shear strength. In addition, damage induced during drilling could not be properly controlled. Moreover, Van der Heever et al. [42] investigated the shear performance of a fiber-reinforced printable concrete under constant confining stress via a direct shear test (based on

ASTM D5607-95 [43]) to evaluate the shear properties of cylindrical specimens considering different interface directions (Fig. 1d). The direction of loading influenced the shear properties, and a non-linear evolution of the shear strength was observed as the confining stress increased.

The test proposed by Napolitano et al. [37], Alchaar et al. [39], Rahul et al. [40], and Meurer et al. [41] allowed to examine the influence of different printing time intervals and environmental conditions on the interlayer shear strength, but they did not consider the effect of confining stress, which corresponds on a larger scale to the vertical loads acting on a structural element (e.g., walls). In contrast, the experimental campaign of Van der Heever et al. [42] considered different intensities of confining stress on the printed specimens, but the tests were carried out on small cylinders consisting of only two layers, with a height and diameter of approximately 2 cm (Fig. 1d), which could cause local effects. Consequently, further studies on the interface shear strength, which consider the presence of different levels of confining stress and a more representative height, are needed.

Generally, the tests used for plain concrete (PC) can be adopted as a reference to assess the shear properties of 3DPC material. The direct shear test, as mentioned by Espeche et al. [44], involves the application of two parallel loads in opposite directions on both sides of the specimen interface. However, a disadvantage of this test is the bending moment due to force eccentricity. To overcome this issue, alternative methods were introduced, including the push-out test, the L-shaped test, and the slant shear test. Giraldo-Soto et al. [45] studied the influence of different experimental configurations on shear transfer capacity in steel fiber-reinforced concrete (SFRC). The study examined the L-shaped test (Fig. 1e) and the push-out test (Fig. 1f). In the case of the L-test configuration, no specific factors were identified that significantly influenced the shear transfer capacity. In contrast, push-out tests without prestressing show the influence of the arch effect, which compressed the shear plane and reduced crack opening with a consequent overestimation of the shear capacity (Fig. 1f). It becomes necessary to implement additional modifications, including the introduction of additional supports at the ends of the specimens to apply prestress, which helps to limit bending effects during testing. Zanotti et al. [46] compared the slant shear test and the push-out test (Fig. 1g). In the slant shear test, interfacial bond failure or compression failure may occur, depending on both the compressive strength of the substrate and overlay, and on the inclination of the interface plane. On the contrary, all specimens in the push-out test showed clear bond failure. Moreover, the test results suggest that the shear strength measured by means of the push-out test can be significantly lower than that measured with the slant shear test. The compressive stresses in this test generate higher interlocking and friction forces, increasing the shear failure load. Additionally, the slant shear test (Fig. 1g) was also adopted by Licciardello et al. [47] to investigate the load-bearing capacity of 3DPC, accounting for the anisotropy of the material caused by printing layers. Forty-five specimens with varying layer inclinations (0°–90°) and a 30-min cold joint were tested to identify the governing parameters of a Mohr failure envelope for 3DPC (the established modified Coulomb yield condition of the concrete is complemented by a Coulomb failure criterion of the layer joints), and two distinct failure modes—matrix failure and layer-interface failure—were identified depending on the layer inclination. The proposed MSST provides a practical method to derive the cohesion and friction parameters of 3DPC layers, offering a base for the design of load-bearing 3D-printed structures.

The choice of the most appropriate test methods for the evaluation of the hardened state properties of 3DPC requires the identification of the predominant loading condition for a given structural element. Among the many that have been investigated by different authors [7, 48–53], little attention was given to the structural behavior of 3D printed walls, which can be subjected to both vertical (compression) and horizontal (shear) actions. With the aim of shedding some more light, this study concerns specifically the determination of the inter-layer shear behavior through the proposal of a new push-out test method which accounts for both compressive and shear stresses.

2 Research significance

The research study aims at investigating the interface behavior of 3D printed concrete layers subjected to the combined action of shear forces and transverse compression, by means of an experimental campaign and numerical analyses. To this end, a new test methodology is proposed, referred throughout the paper as push-out test, adapting shear tests typically used for

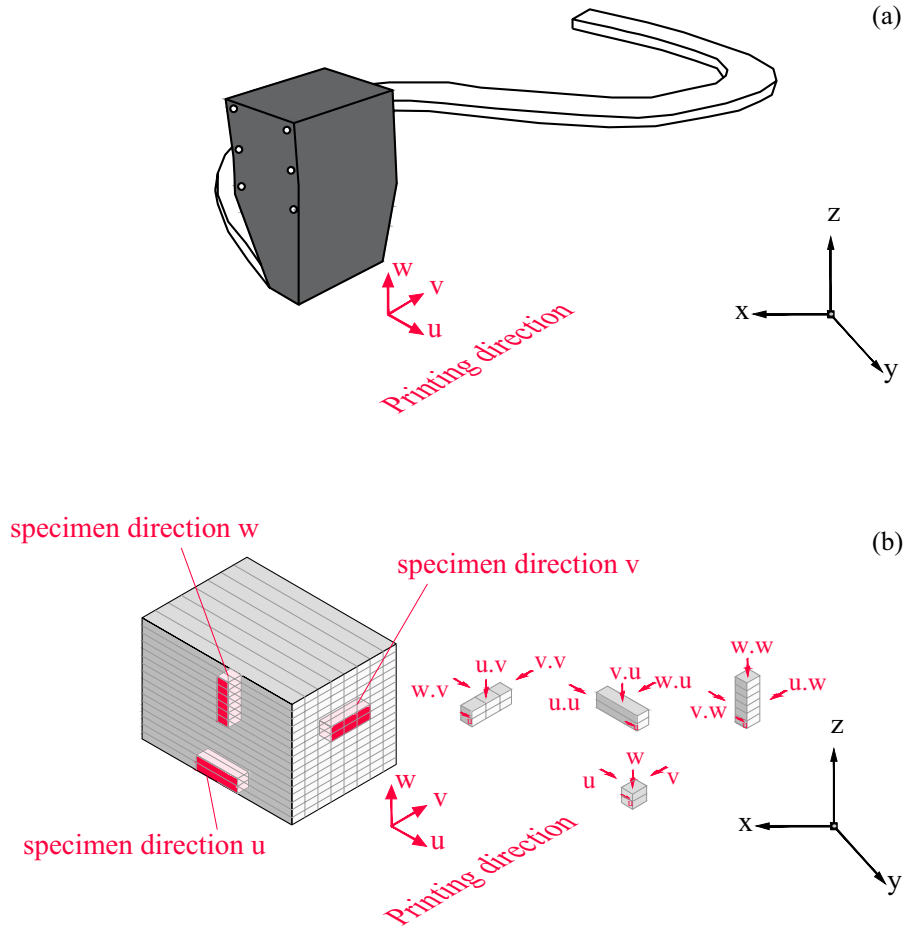

Fig. 2 Different definitions of directionality adapted from Bos et al. [55] (**a**), adapted from Mechtcherine et al. [54] (**b**)

traditional concrete and masonry. The results of these tests provide valuable insights into shear properties, including shear strength, shear stiffness, cohesion, and friction angle. In addition, non-linear numerical analyses based on fracture mechanics through both smeared and discrete crack approaches are proposed and validated against experimental results.

3 Directionality

During the experimental investigation, special attention has been paid to the anisotropy of 3DPC (due to layer deposition), since it could affect the mechanical properties. In the literature, this subject is referred to as directionality, as introduced by Mechtcherine et al. [54]. Available studies on this topic proposed different approaches: Bos et al. [55] defined directionality in printing by means of a system of local coordinates (u, v, w), where u represents the printing direction (Fig. 2a). Subsequently, Mechtcherine et al. [54] presented an extended definition of directionality consisting of two letters: the first denotes the axis of a normal force or the axis of rotation for a bending load, and the second indicates the longitudinal axis of the specimen (Fig. 2b). The convention proposed by Mechtcherine et al. [54], and subsequently adopted in the RILEM TC 304-ADC interlaboratory study [33], is applied also throughout the present work.

4 Experimental programme

4.1 Materials

The 3D printed concrete (3DPC) under investigation was a premixed compound containing quartz sand (with a maximum diameter of 2 mm), cement

(CEM I 52.5R), water, and other admixtures, which ensure a proper rheology during the pumping phase and the capacity to support self-weight by the progressive development of its mechanical properties during the printing phase.

Composition details cannot be disclosed since it is a commercial material under development, and the mix design is patented. Water content on the total weight of the material is 0.15 l/kg.

4.2 Production of the printed specimens

The 3DPC specimens were fabricated and cured in a laboratory under constant environmental conditions, maintaining a temperature of 20 ± 2 °C and a humidity of 80 ± 5%. The specimens were printed using a 6-axis robotic arm connected to a digital system with a programmed 3D printing path. The nozzle of the printing system was circular with a diameter of 28 mm, and the printing speed was set at 250 ± 25 mm/s, resulting in a time interval between successive layers of 30 s to 1 min.

The test specimens were cut by wet-sawing from the walls of a sample with a thickness of 6 cm and a height of 20 cm (20 layers with a layer height of approximately 10 mm), and variable length, as shown in Fig. 3. The testing specimens were extracted approximately 6 months after printing.

The flexural strength of the printed material was measured on beams with nominal dimensions of 160 × 40 × 40 mm (obtained by sawing, see Fig. 4a) and tested along orientation *v.u* and *v.w*, where the symbols denotes the axis of bending rotation and the longitudinal axis of the specimen, respectively, according to the RILEM notation [33] (see Fig. 2b). The tensile strength and the elastic modulus (Fig. 4c) were measured on specimens with nominal dimensions equal to 120 × 60 × 60 mm and tested according to direction *w* (normal stress perpendicular to the printing plane), while the compressive strength was evaluated along both the direction *w* and *u* (Fig. 4b). Concerning shear behavior, the specimens had nominal dimensions of 160 × 120 × 60 mm (Fig. 4d) and were tested along the direction *u* (loading direction inducing stresses parallel to the *u*-axis within the printing plane). Figure 4 depicts specimens and testing set-ups adopted in the experimental campaign. Tests on cast specimens were also performed for reference purposes, which were considered directionally independent.

4.3 Geometry accuracy

As a result of the printing process, the cross-section of the specimens can have significant irregularities with bulging sides, as shown in Fig. 5a. Therefore,

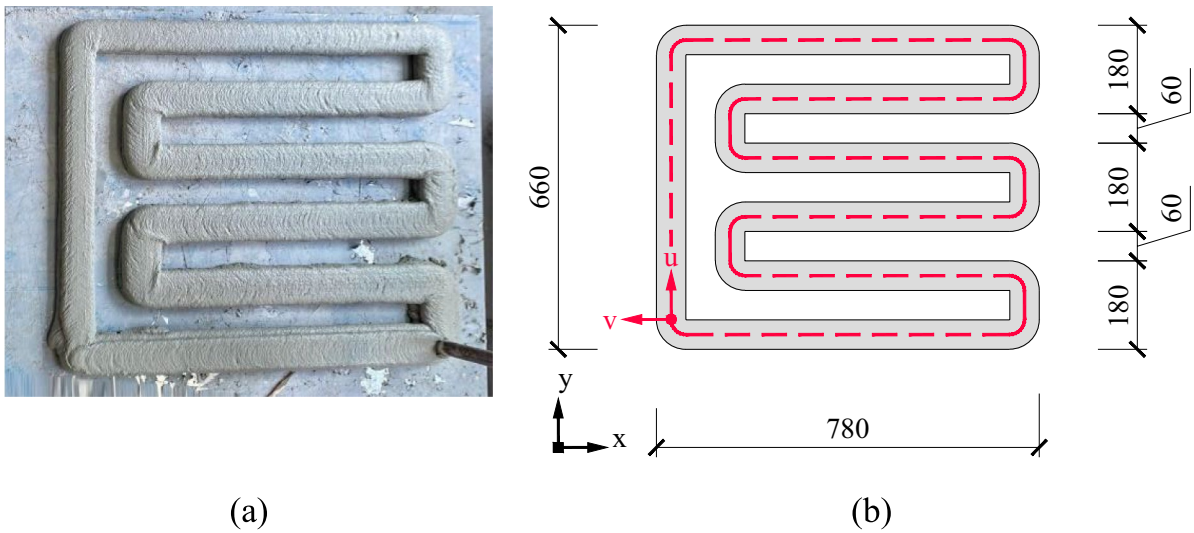

Fig. 3 3DPC specimen in the printing phase (**a**) and its plan view with dimensions (**b**). Measures in millimeters

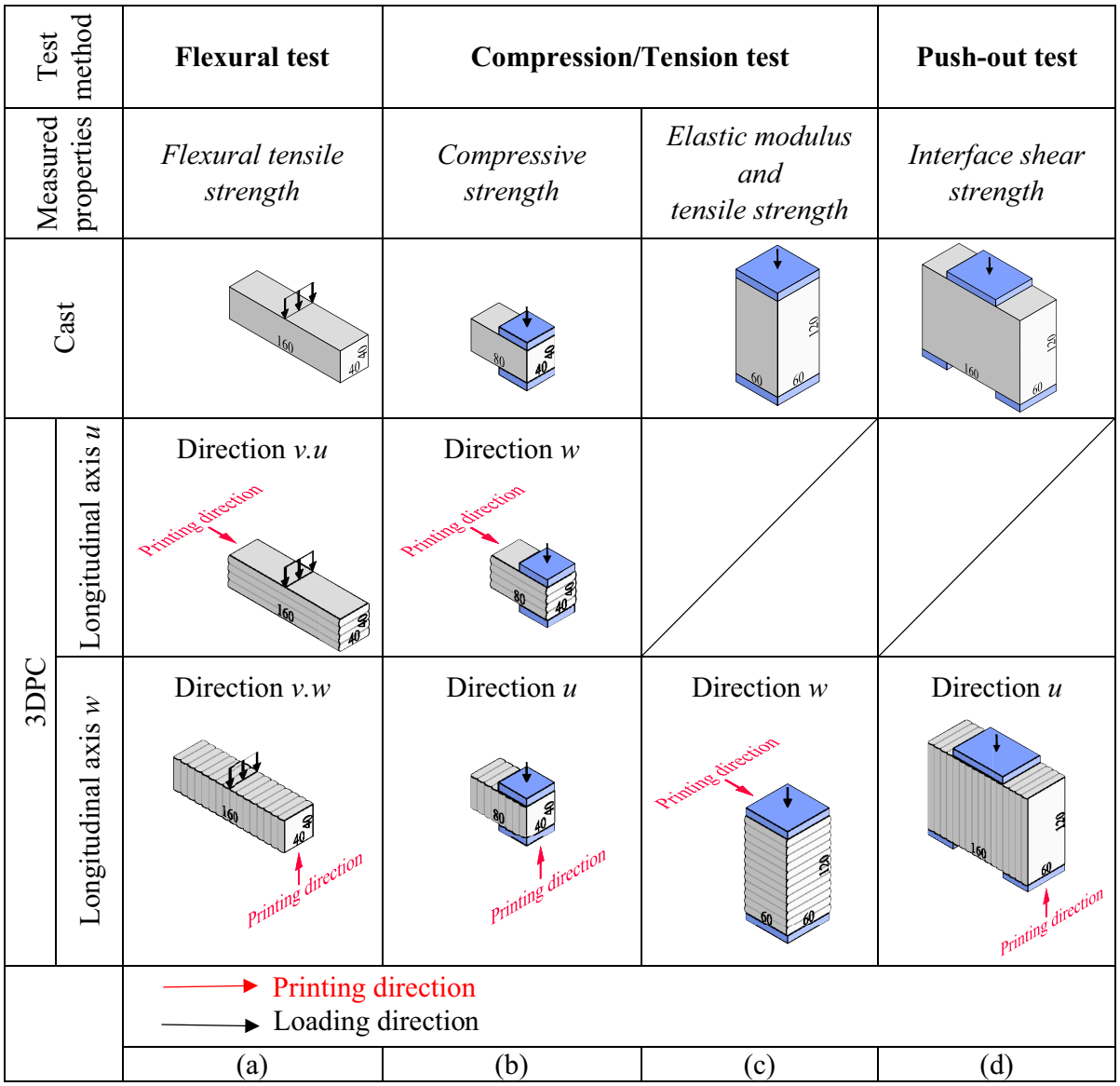

Fig. 4 Characterization of the mechanical properties of 3DPC according to the different directions: flexural test (**a**), compression test (**b**), elastic modulus test and direct tension test (**c**), and push-out test (**d**)

the correct evaluation of the cross-sectional areas is critical in defining the stresses acting in the material. For this purpose, three distinct areas can be defined:

- A_{max} (in red in Fig. 5b) is assessed by considering the maximum wall thickness of the specimen; it results in a general overestimation of the effective resisting cross-sectional area of the specimen:

$$A_{max} = h \cdot t_{max} \quad (1)$$

where h is the height of the specimen and t_{max} is the maximum thickness of the specimen.

- A_{min} (in green in Fig. 5c) is evaluated by considering the minimum wall thickness of the specimen excluding the contribution of the concrete bulging sides:

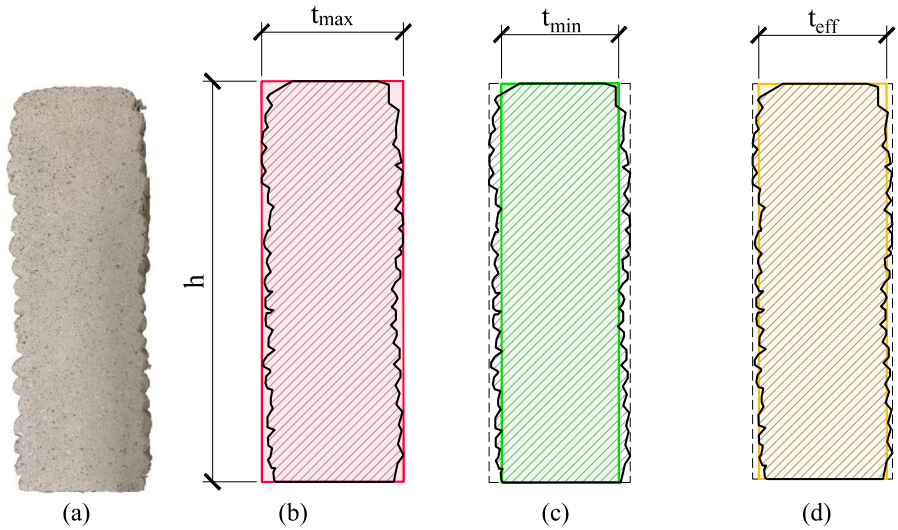

Fig. 5 Accuracy of 3DPC specimens: typical cross-section (**a**), maximum area A_{max} (**b**), minimum area A_{min} (**c**), and effective area A_{eff} (**d**)

$$A_{min} = h \cdot t_{min} \quad (2)$$

where t_{min} is the minimum thickness of the specimen. It should be noted that A_{min} is estimated between 80 and 85% of the maximum area A_{max}.

- A_{eff} (in orange in Fig. 5d) is calculated as the average between A_{max} and A_{min} and is assumed as the effective area of the specimen considering the contribution of the bulging sides. The effective thickness can be calculated as follows:

$$t_{eff} = A_{eff}/h \quad (3)$$

A_{eff} can be estimated at about 90% of the maximum area A_{max}.

For both nominal wall thicknesses (40 mm and 60 mm), the actual thickness variability was quantified by $t_{max,}$ $t_{min,}$ and t_{eff} measured along the specimen. The selection (A_{max}, A_{min}, A_{eff}) of the area depends on whether the concrete bulging sides influence the properties of the material, depending on the specific type of test being carried out. For flexural and compression tests performed in the orientation *v.u* and *u* respectively, the effective area A_{eff} was used, while considering the orientation *v.w* for flexural and *w* for compression tests, the minimum area A_{min} was selected since concrete bulging sides did not contribute to the tensile and compressive strength. For the direct tension test (direction *w*) and push-out test (direction *u*), the minimum area A_{min} was considered for the evaluation of 3DPC strength.

5 Experimental tests

5.1 Flexural test

The flexural strength was evaluated by three-point bending tests according to EN 1015-11:2019 [56] for mortar, which served as a reference. The setup consisted of two steel bearing rollers, and a third roller was centrally placed on top of the specimen for load application (Fig. 6a). The vertical load on the upper section of the specimen was applied by a servo-controlled hydraulic jack with a maximum capacity of 100 kN. The test was carried out under displacement control at a rate of 0.05 mm/min. A total of 9 and 18 tests were carried out for cast and printed material, respectively.

5.2 Compression test

The compressive strength was evaluated according to EN 1015-11:2019 [56] for mortar by placing the specimens (the resulting pieces from the flexural test) between two steel plates with dimensions 40×40 mm (see Fig. 6b). The test was carried out with the same testing machine used for flexural tests under displacement control at a rate of 0.05 mm/min. A total of

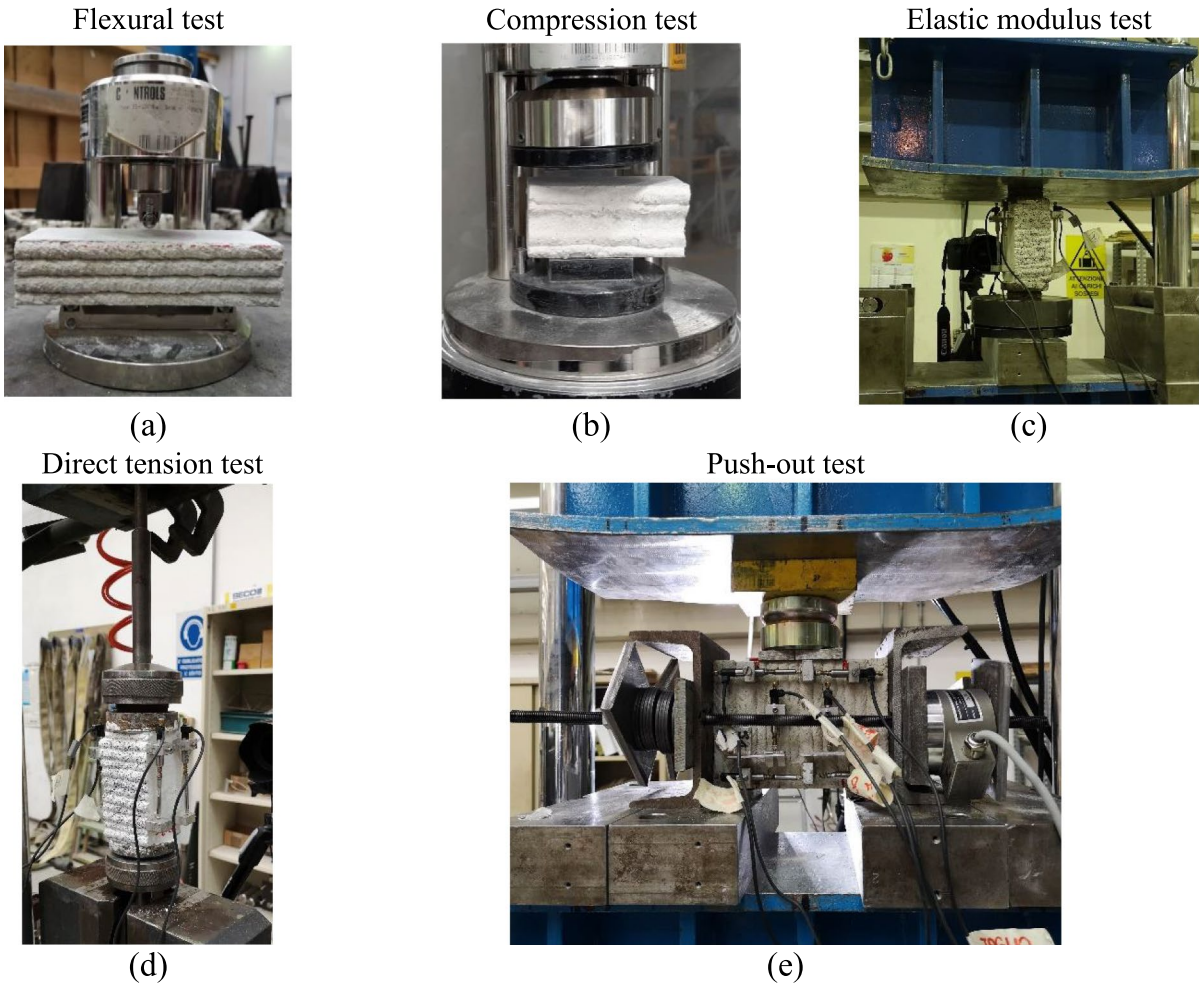

Fig. 6 Test methods: flexural test (**a**), compression test (**b**), elastic modulus test (**c**), direct tension test (**d**), and push-out test (**e**)

18 and 36 tests were carried out for cast and printed material, respectively.

5.3 Elastic modulus test

The compressive modulus of elasticity was measured using a customized procedure developed with reference to the EN 12390-13:2013 [57] standard. The load was applied using a servo-controlled universal testing machine with a maximum capacity of 500 kN (Fig. 6c), and the test was carried out under displacement control at a rate of 0.001 mm/min. Longitudinal strains were measured using four linear variable differential transformers (LVDTs) located at the corners of the specimen. The elastic modulus was determined in compression by applying two cycles, each consisting of three repetitions (the first at 10% and the second at 30% of the maximum load bearable by the sample). A total of 3 and 6 tests were carried out for cast and printed material, respectively.

5.4 Direct tension test

The uniaxial tensile strength was measured by applying the vertical load through a servo-controlled hydraulic jack with a maximum capacity of 100 kN. The specimen was glued with an epoxy resin between two steel plates connected to the testing machine, as shown in Fig. 6d. The test was carried out under displacement control at a rate of 0.001 mm/min. A total of 6 tests were performed for the printed material.

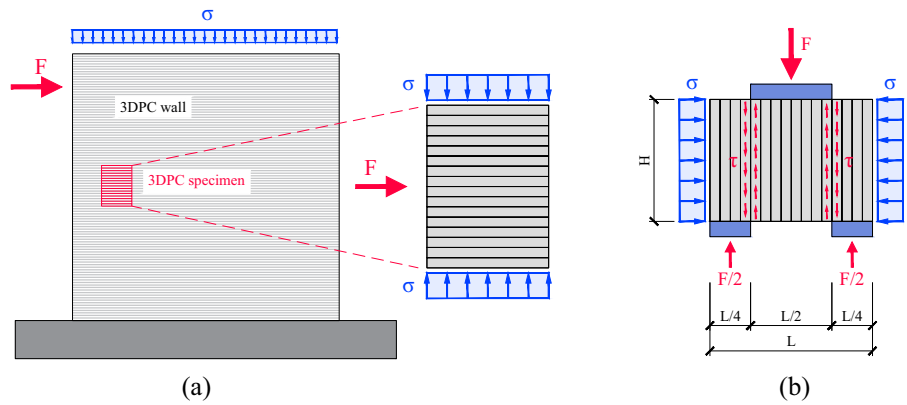

Fig. 7 Schematization of the push-out test: typical shear wall (**a**) and test specimen (**b**)

5.5 Push-out test

The inter-layer shear strength was measured through a new testing methodology derived from the EN 1052-3 [38] standard, concerning the shear strength of masonry elements (push-out test, see Fig. 6e).

5.5.1 Test conceptualization

It should be clarified that, for the sake of simplicity, the push-out test was performed on specimens rotated by 90° with respect to the printing direction. In this new reference system, the vertical load F applied to the specimen represents the lateral load acting on a typical shear wall, while the horizontal stress σ applied to the specimen represents the gravitational load acting on the same wall (see Fig. 7a).

The test was carried out on a prismatic specimen with printed layers placed in the vertical direction, adopting a 3-point loading scheme. Dimensions of the specimen are discussed in detail in Sect. 5.5.2. The vertical loading F was applied in the center of the upper surface through a steel plate covering the central layers (over 1/2 of the specimen length) while supports, consisting of two steel plates, were placed on the sides of the lower surface (over 1/4 + 1/4 of the specimen width; see Fig. 7b). In this configuration, compressive stresses under the loading point and over the supports were equal, while shear failure was forced to develop along the two symmetrical inter-layer surfaces between the loading point and the outer supports. Lateral loading was applied on the sides of the specimen to reach different levels of compressive stress normal to the inter-layer surfaces (*i.e.*, confinement). The testing apparatus is described in Sect. 5.5.3.

5.5.2 Specimen dimensions

The dimensions of the specimen were established to identify the proportions that favor a shear failure on the inter-layer surfaces. To achieve this objective, the 3DPC interface shear strength (τ_i) along the two vertical failure surfaces of the specimen (highlighted in red in Fig. 7b) should be lower than the compressive strength of concrete (f_{cm}) under the loading point (see Fig. 7b), as expressed by the following equation:

$$f_{cm} \cdot (l/2 \cdot t) > \tau_i \cdot 2 \cdot (h \cdot t) \tag{4}$$

where l is the length, h the height, and t the width of the specimen (see Fig. 7b). A series of preliminary tests was carried out to better define the geometry of the specimens. Moreover, a representative height for the test specimen was selected to avoid local shear effects and limit flexure phenomena. The chosen height also permitted an easy test execution, allowing proper positioning of the test instrumentation. However, special attention is required since an excessive specimen height could result in compression failures beneath the loading point, as observed in some preliminary tests [58].

Given the thickness of the 3DPC layer equal to 10 mm and the need to have a number of layers which is a multiple of 4 (to apply the test configuration discussed in Sect. 5.5.1), the length l of the specimen was set to 160 mm, comprising 16 layers, the height h of the specimen was set to 120 mm, and the width t was equal to 60 mm. The central loading length was

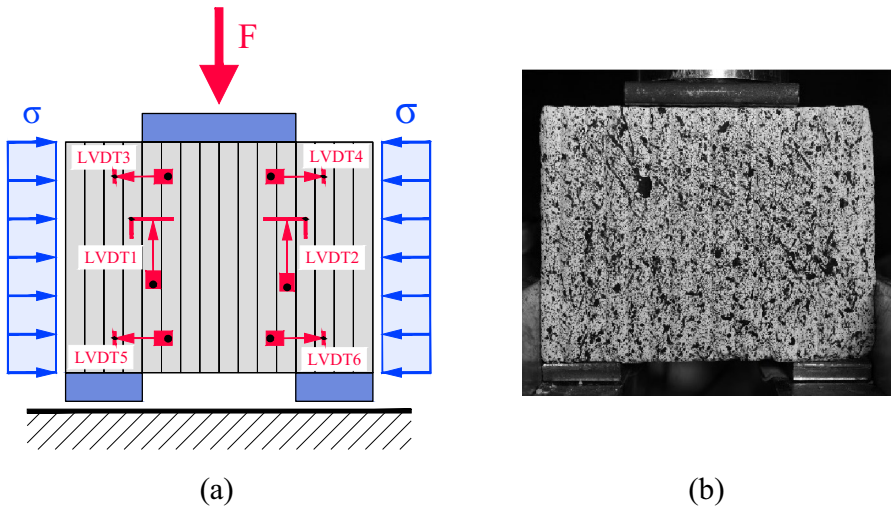

Fig. 8 Instrumentation of the push-out test: LVDTs (**a**) and DIC (**b**)

equal to 80 mm (8 layers), while the support length was equal to (40 + 40) mm (4 + 4 layers).

5.5.3 Test setup

Push-out tests were carried out by monotonically increasing the vertical load up to failure of the specimens with different confinements: (a) without confining stress (0 MPa) and (b) considering three different levels of confining stress, namely 1 MPa, 2 MPa, and 4 MPa, simulating the stress state at the base of a multi-story 3DPC building.

The vertical load was applied by a servo-controlled universal testing machine with a maximum capacity of 500 kN under displacement control, at a rate of 0.05 mm/min. Confining stress was applied using a system consisting of conical disc springs (CB-DIN 2093 60×20.4×2) and two M10 threaded rods. During the test, the normal stress remained constant and was monitored through two load cells placed on each threaded bar and, when necessary, adjusted (Fig. 6e).

On the front side of the specimen, instrumentation included two vertical and four horizontal LVDTs arranged to measure crack opening (Mode I) and relative slip (Mode II) between layers in different locations of the specimen: LVDT1 and LVDT2 were used to measure slip along the left and right critical sections, respectively, while LVDT3, LVDT4, LVDT5, and LVDT6 were used to measure crack opening as shown in Fig. 8a. Digital Image Correlation (DIC) was adopted on the backside of the specimen to detect crack initiation and propagation during the test, as shown in Fig. 8b.

6 Experimental results and discussion

6.1 Mechanical properties

The mean compressive strength f_{cm} of 3DPC specimens was 57 MPa and 55 MPa for directions *u* and *w*, respectively. The mean flexural tensile strength $f_{ctm,fl}$ was equal to 6.85 MPa and 5.35 MPa for orientations *v.u* and *v.w*, respectively. The results are consistent with existing literature [25, 26, 28–31], which indicates negligible differences in compressive strength and significant variation of the flexural strength.

The uniaxial tensile strength (f_{ctm}) in direction *w* was equal to 2.87 MPa, half of the flexural strength. The elastic modulus E_{cm} in direction *w* was equal to 28 GPa, showing a 20% reduction with respect to the expected elastic modulus of an ordinary concrete (35 GPa) with the same strength, according to Eurocode 2 [59]. The main experimental results are summarized in Table 1.

It should be observed that the mechanical properties of cast specimens, having the same mix design, are overall lower than those of the printed specimens, with a 12% reduction in compressive strength, an 8% reduction in flexural strength, and a 10% reduction in the elastic modulus. The higher mechanical properties measured for the 3DPC specimens compared to the cast references are attributed to the extrusion-based deposition,

Table 1 Main mechanical properties of 3DPC: compressive strength, flexural tensile strength, direct tensile strength, elastic modulus, and density (N: number of specimens)

	type			N	Average	St.dev	C.o.v	Direction
Compressive strength	cast	$f_{cm,cast}$	[MPa]	18	50	2.61	6.84	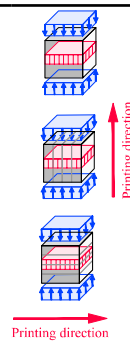
	printed	$f_{cm,u}$	[MPa]	36	57.05	8.91	15.6	
	printed	$f_{cm,w}$	[MPa]	36	54.68	11.64	21.3	
Flexural tensile strength	cast	$f_{ctm,fl,cast}$	[MPa]	9	6.27	0.65	10.4	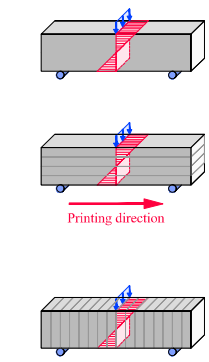
	printed	$f_{ctm,fl,v.u}$	[MPa]	18	6.85	1.09	15.9	
	printed	$f_{ctm,fl,v.w}$	[MPa]	18	5.35	1.48	27.6	
Uniaxial tensile strength	printed	$f_{ctm,w}$	[MPa]	6	2.87	0.35	12	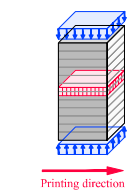
Elastic modulus	cast	$E_{cm,cast}$	[MPa]	3	25,025	1731	6.9	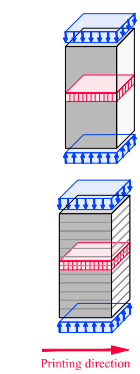
	printed	$E_{cm,w}$	[MPa]	6	27,762	785	2.8	
Density	cast	ρ_{cast}	[kg/m^3]	9	1997	16	0.8	
	printed	$\rho_{v.u}$	[kg/m^3]	18	2226	211	9.5	
	printed	$\rho_{v.w}$	[kg/m^3]	18	2170	168	7.7	

which promotes a more consistent compaction of the fresh material than manual placement in the molds. As a result, the cast specimens exhibited, on average, a 10% lower density. This lower density is consistent with their reduced compressive strength and elastic modulus.

6.2 Shear behavior

The push-out tests were carried out on a total of 12 specimens, with three samples for each confinement level. Figure 9 shows interface shear stress versus slip curves for 3DPC specimens with and without confinement. A qualitative representation (*i.e.*, contour plot) of the strains at the end of the test is provided for each graph, as obtained from DIC.

Numerical values of the most significant performance indicators obtained from experimental results are summarized in Table 2. The latter includes the specimen nomenclature (ID), which indicates the type of manufacture (P for printed), the level of confinement (0 to 4 MPa), and the name of the specimen. In addition, key indicators such as maximum force (F_{max}), minimum effective area (A_{min}), confinement level (σ_n), interface shear strength ($\tau_{i,u}$ where i stands for the interface and u the loading direction), shear stiffness (k_s) and observed failure mode are reported.

The average interface shear strength ($\tau_{i,u}$) ranged between 6.24 and 11.23 MPa for confining stress (σ_n) increasing from 0 to 4 MPa, resulting in the increase of interface shear strength with confining stress. All the printed specimens showed an interlayer failure (IF), with a main crack concentrated at the interfaces between the concrete layers (see Fig. 9). Furthermore, the average shear stiffness (k_s), calculated before cracking on the ascending branch of each single curve between 10 and 30%

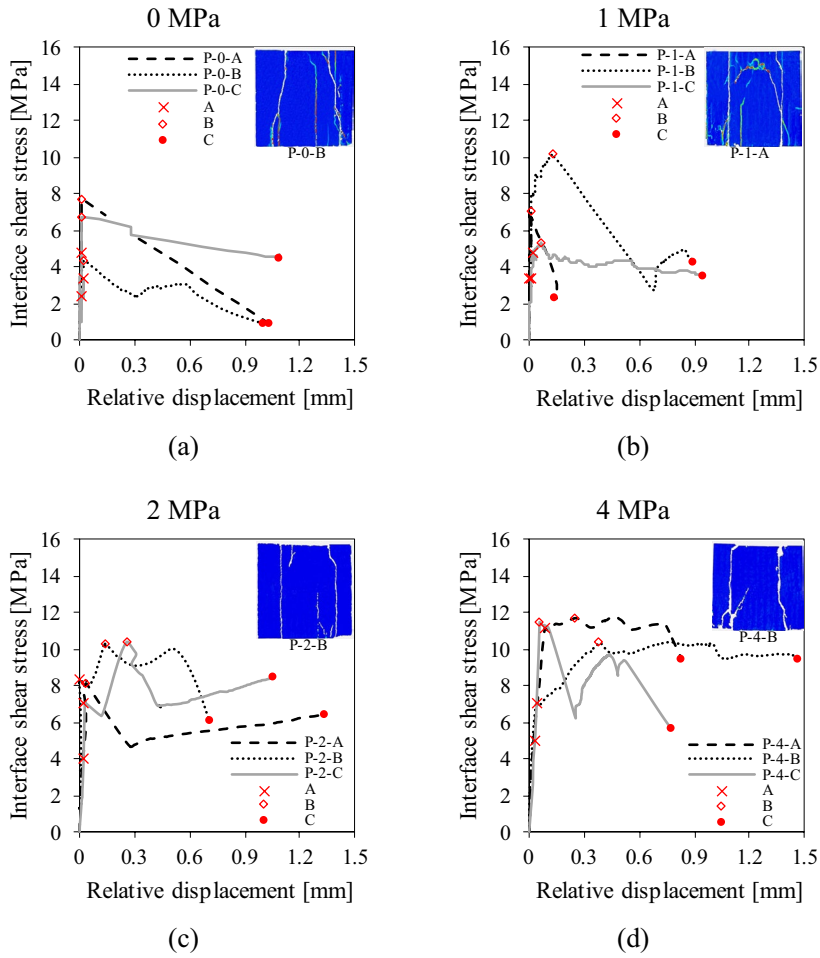

Fig. 9 Interface shear stress versus slip curves of 3DPC specimens from push-out test for the different confining stresses: 0 MPa (**a**), 1 MPa (**b**), 2 MPa (**c**), and 4 MPa (**d**)

Table 2 Summary of the results of the push-out tests carried out on printed specimens

ID [-]	σ_n [MPa]	A_{min} [mm^2]	F_{max} [kN]	$\tau_{i,u}$ [MPa]	k_s [N/mm^3]	Failure mode [-]
P-0-A	0	7011	107.1	7.63	449	IF
P-0-B		6783	58.9	4.34	229	IF
P-0-C		6710	90.7	6.76	114	IF
Mean value (st.dev)				**6.24** (1.70)	**264** (170)	
P-1-A	1	6776	94.9	7.00	300	IF
P-1-B		6783	137.7	10.15	307	IF
P-1-C		6960	73.5	5.28	255	IF
Mean value (st.dev)				**7.48** (2.46)	**287** (28)	
P-2-A	2	6636	108.2	8.15	306	IF
P-2-B		6685	138.0	10.32	–	IF
P-2-C		6698	139.6	10.42	172	IF
Mean value (st.dev)				**9.63** (1.28)	**239** (95)	
P-4-A	4	6840	160.8	11.75	307	IF
P-4-B		6832	142.5	10.43	281	IF
P-4-C		6897	158.9	11.52	182	IF
Mean value (st.dev)				**11.23** (0.70)	**257** (66)	

Bold value represents the mean value of the results of the three specimens (A, B, C) listed above the mean values

of the interface shear strength, ranged between 239 and 287 N/mm^3 regardless of the confining stress.

From the shear stress–relative displacement curves shown in Fig. 9, together with the strain contour plots obtained by DIC (Fig. 10), presented here for specimen P-2-C and similar for the other specimens, three main phases can be identified:

- *Pre-cracking phase* (from origin to point A): the specimens show an elastic behavior, meaning that an increase in load results in a proportional increase of deformation. The first crack occurred at point A (see Fig. 10a).
- *Cracking phase* (from point A to point B): a non-linear behavior is observed and, at the maximum load (point B), the first critical crack appeared on one side of the specimen (Fig. 10b).
- *Post-cracking phase* (from point B to point C): a post-peak behavior is observed, indicating the evolution of the cracking process, ending with the formation of a second critical crack on the opposite side of the specimen (Fig. 10c). Beyond point C, equilibrium is no longer possible, and the specimen collapses in a brittle mode.

As shown in Fig. 11, push-out tests were also carried out on cast specimens. However, the results were omitted because they were considered not representative for characterizing the shear behavior of cast concrete. In fact, while printed specimens

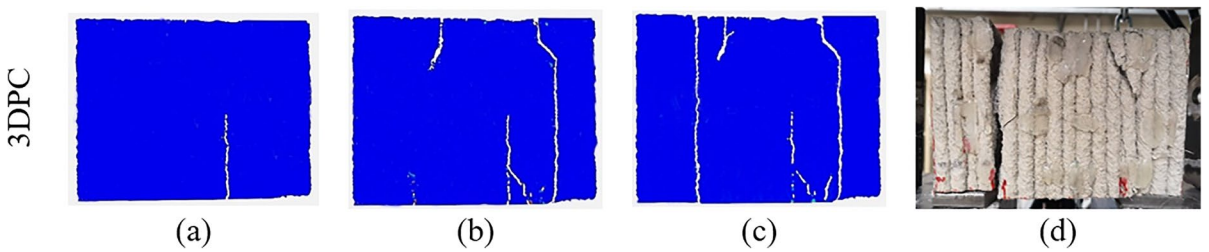

Fig. 10 Typical strains development (by means of contours plot) at formation of the first crack (**a**), at the peak load (**b**), at failure (**c**), and image of the tested specimen P-2-C at failure (**d**)

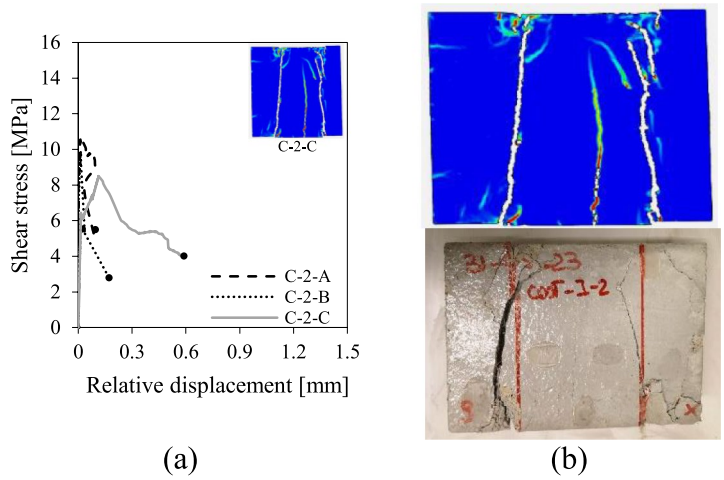

Fig. 11 Typical shear stress versus slip curve (**a**) and crack pattern at failure (diagonal failure) of a cast specimen (**b**)

showed interlayer failure (IF), consistent with the inherently weaker interlayer bonding in extrusion-based 3D printed concrete, cast specimens exhibited compressive diagonal failure (DF), due to the development of an arch mechanism in which the diagonal strut undergoes compressive failure (Fig. 11).

In addition, considering a simple Mohr–Coulomb failure envelope, the cohesion c and friction angle ϕ can be derived from a linear regression of the experimental data (see Fig. 12), with a vertical-axis intercept of 5.83 MPa and an inclination angle of 57°, respectively.

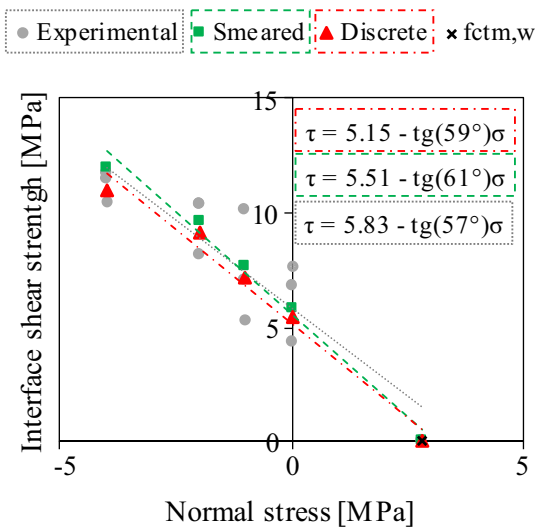

Fig. 12 Mohr–Coulomb failure envelopes: experimental results (dark grey), numerical results with smeared crack approach (green), and discrete crack approach (red).

7 Numerical analyses

Given the layered structure of the 3DPC, conventional modeling methods for masonry and other layered structures may serve as valuable references [60–62]. In this study, two distinct modeling approaches have been employed: the smeared crack approach and the discrete crack approach. With regard to the smeared crack approach, the overall behavior of the element was simulated without any differentiation between filament layers and interface regions, treating the material as a continuum. On the contrary, the discrete cracking approach examined the behavior of the elements by considering each component (filament and interface) individually. In masonry structures, this involves modeling bricks with continuum elements and joints with interface elements; similarly, for 3DPC elements, the layers are represented by continuum elements interconnected by interface elements.

The commercial FE analysis software DIANA FEA (release 10.6) [63] was used to simulate the push-out test. The modeling of the push-out test with the smeared crack approach employed the Total Strain Based Crack Model. In addition, the discrete crack approach used the combined Cracking-Shearing-Crushing Model [64], also known as composite interface model.

7.1 Geometrical properties

To take advantage of symmetry, only half of the specimen was modeled. The specimens had a nominal

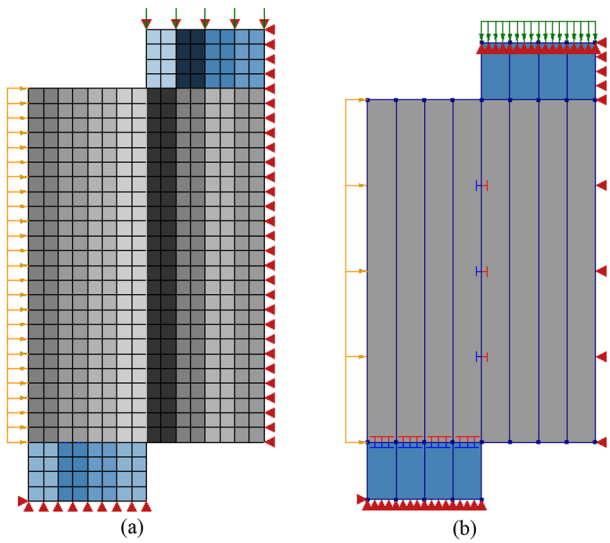

Fig. 13 Push-out test on 3D printed specimens: (**a**) mesh size; (**b**) geometry and boundary conditions

height of 120 mm, length of 160 mm, and width of 60 mm; the layer thickness was 10 mm (Fig. 13). A 2D plane stress model was chosen by assuming a uniform stress distribution along the thickness of the specimen. Moreover, 40 mm × 60 mm steel plates were modeled beneath the loading point and at the bottom of the specimen to provide support. Four-node quadrilateral elements (Q8MEM) were used to simulate concrete and steel elements. Linear interface elements (L8IF) were used to simulate both the steel–concrete interface and the concrete-concrete interface layers (only in the discrete crack approach). A 5 × 5 mm^2 square mesh was used (Fig. 13a). A mesh sensitivity analysis identified these dimensions as the right balance between reliability of results and efficiency of analysis.

7.2 Boundary conditions

The constraints and loads applied are shown in Fig. 13b. The boundary conditions included vertical (in the Y direction) and horizontal (in the X direction) translation constraints on the bottom surface of the supporting steel plate. Because of symmetry, horizontal constraints were also applied along the axis of symmetry of the specimen. The upper load block was subjected to a downward vertical displacement of increasing amplitude. In addition, various levels of confinement (0 MPa, 1 MPa, 2 MPa, and 4 MPa) were applied through a distributed load on the lateral surface of the specimen.

7.3 Steel to concrete interface

Interface elements were used for the contact surface between the specimens and the steel support at the bottom. A Coulomb friction interface model was assumed to represent a condition as realistic as possible; in fact, when the cracking process starts, it allows sliding between the concrete and the steel plates, although to a minimal extent. This interface type is defined by the cohesion (0 MPa), the friction angle (10°), and the dilatancy angle (0°). The values of normal and shear stiffness of the contact surface were set at 10^9 N/mm^3 and 10 N/mm^3, respectively. Steel plates were modeled with linear elastic behavior, characterized by an elastic modulus of 210 GPa and a Poisson's ratio of 0.3.

7.4 Smeared crack approach

The push-out test was modeled considering 3DPC mechanical properties discussed in Sect. 6.1, and by also adopting analytical formulations available in the literature. With reference to the smeared crack approach, the Total Strain Based Crack Model [65] was used to define tensile and compressive behavior of concrete. The stress–strain relationship can be either rotating or fixed, determining whether the crack orientations are constantly fixed or continuously adapt to the principal direction of the strain vector. A rotating crack model was used herein, which implies that cracks reorient as the test proceeds. The input

data for the Total Strain Based Crack Model consists of basic properties of 3DPC experimentally determined (see Table 1), like the Young's modulus $E_{cm,w}$, the tensile strength $f_{ctm,w}$ and the compressive strength $f_{cm,w}$. In addition, the definition of the tensile behavior of 3DPC with a multilinear tensile curve and of the compressive behavior with a parabolic relationship requires additional parameters obtained from empirical formulations. These include the Mode I fracture energy G_f^I(Sect. 7.4.1), the fracture energy in compression G_c, the strain at peak compressive strength α_c, and the crack bandwidth h (Sect. 7.4.2).

7.4.1 Constitutive law for 3DPC in tension

Uniaxial tensile behavior of 3DPC has been modeled by the multilinear tensile curve proposed by fib Model Code 2010 [66] (see Fig. 14a), given the tensile strength $f_{ctm,w}$, as reported in Table 1, and the Mode I fracture energy, as defined by the following equation [66]:

$$G_f^I = 73\left(f_{cm}\right)^{0.18} \tag{5}$$

where f_{cm} is the compressive strength, experimentally determined (equal to $f_{cm,\,w,}$ Table 1).

7.4.2 Constitutive law for 3DPC in compression

Uniaxial compressive behavior has been described by a parabolic relationship (see Fig. 14b), on the basis of the experimental compressive strength $f_{cm,w}$ reported in Table 1. Moreover, the fracture energy in compression G_c was assumed to be about 70 times the Mode I fracture energy G_f^I [67], and the strain in correspondence of the peak compressive strength α_c was estimated as [67]:

$$\alpha_c = \frac{5}{3}\frac{f_{cm,w}}{E_{cm,w}} \tag{6}$$

where $E_{cm,w}$ is the elastic modulus of concrete. A further parameter to be considered is the crack bandwidth h defined by Rots [68] for two-dimensional elements as follows:

$$h = \sqrt{2 \cdot A} \tag{7}$$

where A is the total area of the bi-dimensional finite element.

7.5 Discrete crack approach

In order to deepen the understanding of the behavior of interfaces between consecutive layers in the overall structural response of 3DPC elements, a discrete crack approach was adopted to consider the interface region and concrete layers separately.

The interface elastoplastic constitutive model introduced by Rots and Laurenco [64], known as the combined Cracking-Shearing-Crushing model or the combined interface model for unreinforced masonry, has been adopted in the numerical study (Fig. 14c). The domain is enclosed by a composite yield surface, which includes a tension cut-off for tensile failure (Mode I), a Coulomb friction envelope for shear (Mode II), and a model for compression failure defined by Rots and Laurenco [64] as cap model. The parameters of the constitutive model—such as the tensile strength $f_{ctm,w}$, the compressive strength $f_{cm,w}$, cohesion c, friction angle ϕ, and shear stiffness modulus k_{sc}—were derived from experimental results (see Table 1 and Section 6.2). In addition, the model requires parameters estimated through empirical formulations by following the recommendations of Laurenco [69], including the Mode I fracture energy G_f^I, the dilatancy angle ψ, the Mode II fracture energy G_f^{II}, and the elastic normal stiffness k_{nc}.

The tension cut-off is characterized by the tensile strength $f_{ctm,w}$ (see Table 1) and the Mode I fracture energy, which is calculated according to Eq. (5) [66]. The Coulomb friction envelope is defined through the cohesion c and the friction angle ϕ (which is assumed constant [69]). Furthermore, the shear (Mode II) fracture energy G_f^{II}, which depends on the level of normal stress acting on the interface-layer, is assumed to have an average value equal to 1/10 of cohesion c [69] since the push-out test setup does not allow an accurate estimation of the shear fracture energy of Mode II G_f^{II}. The compressive behavior is described through the compressive strength $f_{cm,w}$ (see Table 1) and the coefficient C_s, which defines the shape of the elliptical cap and is estimated by the following expression [69]:

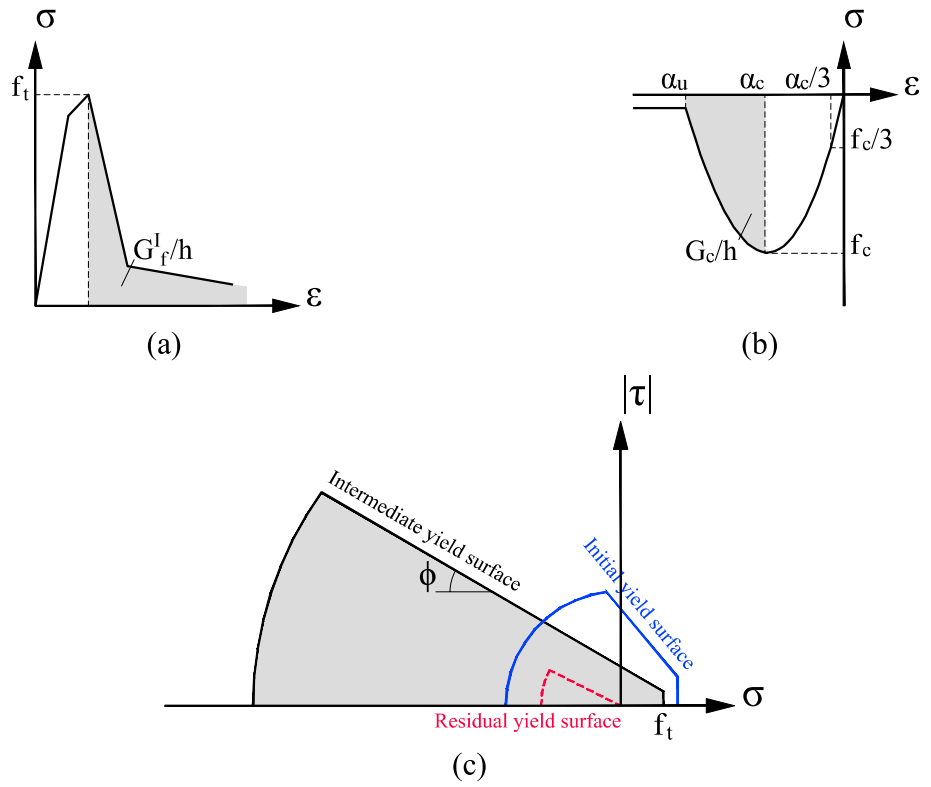

Fig. 14 Material constitutive law adopted for the modeling of the push-out test [65]: tensile behavior (**a**), compressive behavior (**b**), interface material model (**c**)

$$C_s < \sqrt{\frac{f_{cm,w}}{c}} \tag{8}$$

It should be noted that the compressive behavior at the interface was not considered relevant since the objective of the study is to characterize the behavior of the interface under shear actions. Finally, the elastic shear stiffness k_{sc} was set equal to a constant value of 265 N/mm^3 (see Table 2), which represents the average value of the experimental results regardless of the confinement level, since no experimental dependence was observed for the stiffness at the interface. The elastic normal stiffness k_{nc} is determined according to [62]:

$$k_{nc} = k_{sc} \cdot 2 \cdot (1 + \nu) \tag{9}$$

Table 3 summarizes the mechanical properties considered in the models, both in the smeared and the discrete crack approaches.

7.6 Numerical results

Numerical results are presented as interface shear stress vs. slip curves in Fig. 15 for both the smeared crack approach (SCA) and the discrete crack approach (DCA), for each confining stress considered in the experimental campaign (0 MPa, 1 MPa, 2 MPa and 4 MPa).

The numerical predictions from SCA (represented by a black dashed line in Fig. 15) provide a good approximation of experimental curves; in fact, the model accurately describes the linear (pre-peak) behavior and the maximum interface shear strength. Following the peak, a softening phase aligns well with experimental data. As interface slip arises from crack formation, the model adeptly captures the abrupt stiffness reduction when macro-cracks propagate. The accuracy of the SCA model increases with the confinement level.

As far as the numerical results obtained from DCA (represented as a black dotted line in Fig. 15)

Table 3 Input parameters for the numerical models

Smeared crack approach	Elastic modulus	$E_{cm,w}$	[MPa]	28,000
	Poisson ratio	ν	–	0.2
	Crack orientation	–	–	rotating
	Tensile strength	$f_{ctm,w}$	[MPa]	2.9
	Fracture energy mode I*	G_f^I	[N/mm]	0.15
	Compressive strength	$f_{cm,w}$	[MPa]	55
	Compressive fracture energy*	G_c	[N/mm]	10
	Strain at peak*	α_c	‰	3.3
Discrete crack approach	Normal stiffness modulus*	k_{nc}	[N/mm^3]	640
	Shear stiffness modulus	k_{sc}	[N/mm^3]	265
	Tensile strength	$f_{ctm,w}$	[MPa]	2.9
	Fracture energy mode I*	G_f^I	N/mm	0.15
	Cohesion	c	[MPa]	6
	Friction angle	ϕ	[°]	57
	Dilatancy angle	ψ	[°]	0
	Fracture energy mode II*	G_f^{II}	[N/mm]	0.6
	Compressive strength	$f_{cm,w}$	[MPa]	55
	factor C_s*	C_s	–	3

*those properties were evaluated through empirical formulas or established literature

are concerned, a good representation of experimental results is observed as well, both in terms of shear stiffness and maximum interface shear strength. The post-peak behavior is also well represented, where a rapid drop in strength after crack initiation is observed.

Therefore, both methodologies accurately capture the behavior of specimens under push-out testing, but a more stable post-peak behavior seems to be observed in DCA models. Table 4 presents a comparison between the maximum interface shear strength and shear stiffness as obtained from experiments and numerical analysis. As far as the interface shear strength is concerned, the differences between experimental results and numerical predictions are limited to about 15% and can be considered acceptable. On the other hand, the shear stiffness is overestimated by approximately 40% by the smeared crack approach, which is reasonable as this approach does not consider the presence of failure at the interface. In contrast, the discrete crack model underestimates the stiffness by about 20%.

7.7 Failure criterion

The comparison between experimental and numerical results is also discussed with a linear regression on the interface shear strength versus normal stress (i.e., confining stress) plane. Experimental results can be represented by a Mohr–Coulomb failure envelope with a cohesion equal to 5.83 MPa and a friction angle equal to 57° (dark grey line in Fig. 12). By adopting the same failure criterion, SCA and DCA numerical models provide a cohesion (5.51 and 5.15 MPa) and a friction angle (61° and 59°), consistent with the experimental results (green line and red line in Fig. 12 for SCA and DCA models, respectively).

8 Concluding remarks

Unlike traditional concrete, which can be considered as an isotropic material, the 3DPC made by extrusion is characterized by a layered structure due to its construction process. The behavior of interfaces under combined shear and normal actions has been deeply investigated by means of a novel testing methodology and advanced numerical tools based on smeared and discrete crack approaches. From the experimental and numerical results presented herein, the following conclusions can be drawn:

- due to the layered structure of 3DPC, conventional test methods for concrete are not always adequate. Therefore, a new push-out test method

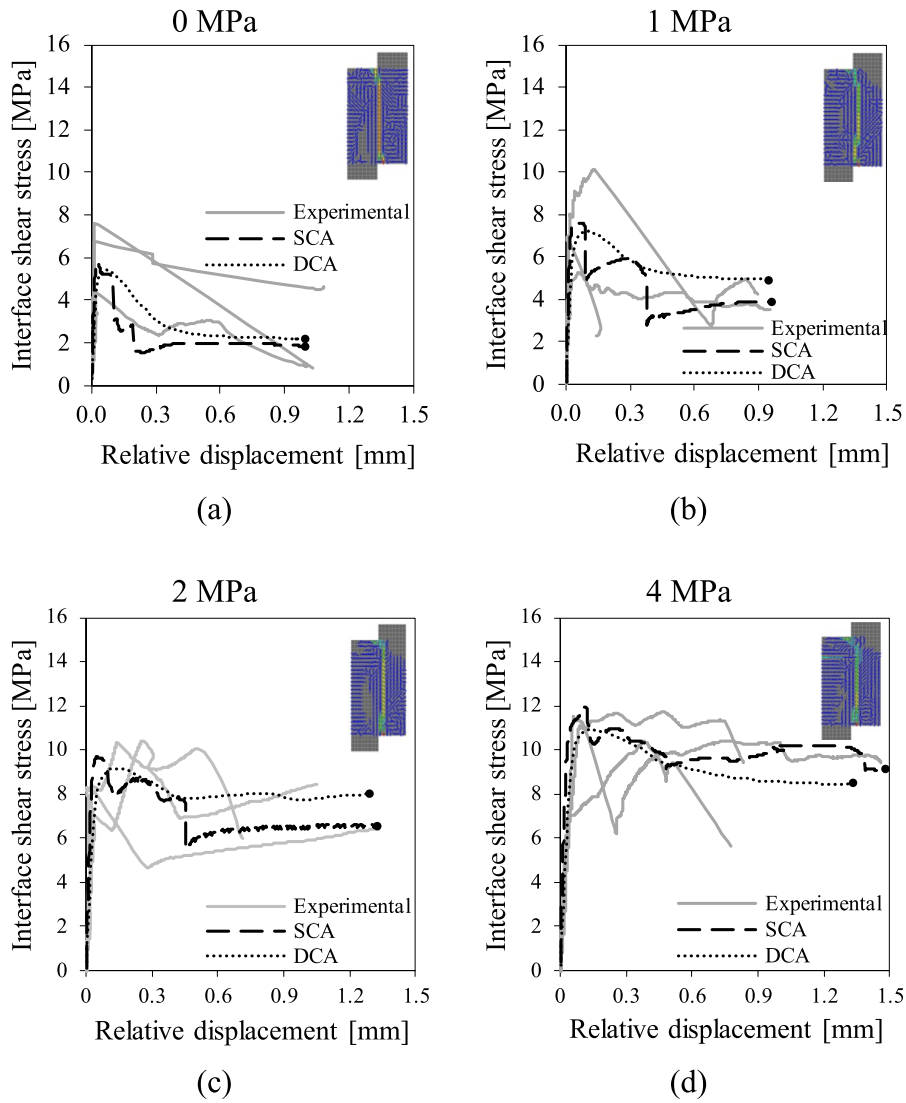

Fig. 15 Interface shear stress vs. slip as obtained with the smeared crack approach (SCA) and the discrete crack approach (DCA): 0 MPa (**a**), 1 MPa (**b**), 2 MPa (**c**), and 4 MPa (**d**) confining stress

Table 4 Maximum experimental interface shear strength $\tau_{i,u}$, shear stiffness k_s, and comparison with the numerical results for different confinement level σ_n

σ_n [MPa]	$\tau_{i,u}$ [MPa]			k_s [N/mm^3]		
	Experiment	SCA	DCA	Experiment	SCA	DCA
0	6.24	5.84(−7%)	5.40 (−14%)	264	420(+38%)	212(−20%)
1	7.48	7.61(+2%)	7.18 (−4%)	287	444(+35%)	212(−26%)
2	9.63	9.68(+1%)	9.16 (−5%)	239	406(+41%)	212(−12%)
4	11.23	11.93(+6%)	10.93 (−3%)	257	343(+25%)	212(−18%)

is proposed to investigate the shear behavior of interfaces between layers, by considering different levels of transverse confinement (0 MPa, 1 MPa, 2 MPa, and 4 MPa). All the tests (three tests for each confinement level considered) showed an interface failure with a well-defined crack concentrated at the interface between concrete layers. The interface shear strength $\tau_{i,u}$ varied between 6.24 and 11.23 MPa, linearly increasing with the level of confining stress. The

shear stiffness was little influenced by the level of confinement. Experimental results can be approximated by a Mohr–Coulomb failure envelope with a cohesion equal to 5.83 MPa and a friction angle equal to 57°.

- Numerical simulations of push-out tests were validated against experimental results with the aim of developing valuable tools for the modeling of larger-scale 3DPC structural elements and buildings. Non-linear finite element analyses, based on both smeared crack approach (SCA) and discrete crack approach (DCA), provided satisfactory approximation of the experimental results in terms of elastic stiffness, interface shear strength, and post-cracking behavior. By adopting the Mohr–Coulomb envelope, numerical results provided a good approximation of the cohesion and of the friction angle.

Acknowledgements The authors gratefully acknowledge Elisa Carleschi and Serena Massari for their support in the ideation of the experimental setup, and Ivan Beltracchi for his assistance with the numerical analysis. Special thanks to technician Andrea Del Barba for his help during the experimental tests. The authors also thank Heidelberg Materials for providing the material, and Professor Costantino Menna and ETE-SIAS for their support in printing the specimens. No funding was received for conducting this study.

Author contributions Lucia Licciardello Conceptualisation, Methodology, Investigation, Data curation, Writing—Original Draft, Writing—Review & Editing; Adriano Reggia Conceptualisation, Methodology, Investigation, Data curation, Writing—Original Draft, Writing—Review & Editing; Giovanni Metelli Conceptualisation, Methodology, Writing—Review & Editing. Giovanni Plizzari Conceptualisation, Writing—Review & Editing.

Funding Open access funding provided by Università degli Studi di Brescia within the CRUI-CARE Agreement. No funding was received for conducting this study.

Data availability The data that support the findings of this study are available from the corresponding author upon reasonable request.

Declarations

Conflict of interest The authors declare that they have no conflict of interest.

References

1. De Schutter G, Lesage K, Mechtcherine V, Nerella VN, Habert G, Agusti-Juan I (2018) Vision of 3D printing with concrete — Technical, economic and environmental potentials. Cem Concr Res 112:25–36. https://doi.org/10.1016/j.cemconres.2018.06.001
2. Menna C, Mata-Falcón J, Bos FP, Vantyghem G, Ferrara L, Asprone D et al (2020) Opportunities and challenges for structural engineering of digitally fabricated concrete. Cem Concr Res 133:106079. https://doi.org/10.1016/j.cemconres.2020.106079
3. Italcementi https://www.italcementi.it/it/casa-stampata-3D
4. Weger D, Stengel T, Gehlen C, Maciejewski Y, Meyer-Brötz F (2021) Approval for the construction of the first 3D printed detached house in Germany—significance of large scale element testing. In: Jones SZ, Kreiger EL (eds) Standards development for cement and concrete for use in additive construction, ASTM International, pp 144–69. https://doi.org/10.1520/STP163620200119
5. PERI https://www.peri.com/en/media/press-releases/germanys-first-printed-house-officially-openend.html
6. The Wave House data center https://cobod.com/heidelberg-inaugurates-europes-largest-3d-printed-building-the-wave-house-data-center/
7. Salet TAM, Ahmed ZY, Bos FP, Laagland HLM (2018) Design of a 3D printed concrete bridge by testing. Virtual Phys Prototyp 13:222–236. https://doi.org/10.1080/17452759.2018.1476064
8. Wolfs R (2021) A framework for large-scale structural applications of 3D printed concrete. https://doi.org/10.5446/56115
9. Dell'Endice A, Bodea, Van Mele T, Block P (2024) Striatus 2.0: Phoenix—Improving circularity of 3D-concrete-printed unreinforced masonry structures. Fabricate 2024: Creating Resourceful Futures, UCL Press, n.d., pp 90–7
10. Lloret E, Shahab AR, Linus M, Flatt RJ, Gramazio F, Kohler M et al (2015) Complex concrete structures. Comput Aided Des 60:40–49. https://doi.org/10.1016/j.cad.2014.02.011
11. Lloret Fritschi E (2016) Smart dynamic casting–a digital fabrication method for non-standard concrete structures. Doctoral Thesis. ETH Zurich, https://doi.org/10.3929/ethz-a-010800371
12. Lloret-Fritschi E, Reiter L, Wangler T, Gramazio F, Kohler M, Flatt RJ (2017) Smart dynamic casting: slip-forming with flexible formwork–Inline measurement and control. https://doi.org/10.3929/ETHZ-B-000219663

13. Lloret-Fritschi E, Scotto F, Gramazio F, Kohler M, Graser K, Wangler T et al (2019) Challenges of real-scale production with smart dynamic casting. In: Wangler T, Flatt RJ (eds) First RILEM international conference on concrete and digital fabrication—digital concrete 2018, vol 19. Springer International Publishing, Cham, pp 299–310. https://doi.org/10.1007/978-3-319-99519-9_28
14. Dörfler K, Hack N, Sandy T, Giftthaler M, Lussi M, Walzer AN et al (2019) Mobile robotic fabrication beyond factory conditions: case study Mesh Mould wall of the DFAB HOUSE. Constr Robot 3:53–67. https://doi.org/10.1007/s41693-019-00020-w
15. Anton A, Lin CW, Skevaki E, Wang M, Wangler T, Flatt R et al (2024) Tor Alva: A 3D Concrete Printed Tower. UCL Press, Fabricate 2024
16. Soto AG, Gebhard L, Anton A, Dillenburger B, Kaufmann W (2024) Structural testing campaign for a 30 m tall 3D printed concrete tower. In: Lowke D, Freund N, Böhler D, Herding F (eds) Fourth RILEM international conference on concrete and digital fabrication, vol 53. Springer Nature Switzerland, Cham, pp 493–500. https://doi.org/10.1007/978-3-031-70031-6_57
17. Roussel N (2018) Rheological requirements for printable concretes. Cem Concr Res 112:76–85. https://doi.org/10.1016/j.cemconres.2018.04.005
18. Wolfs RJM, Bos FP, Salet TAM (2018) Early age mechanical behaviour of 3D printed concrete: numerical modelling and experimental testing. Cem Concr Res 106:103–116. https://doi.org/10.1016/j.cemconres.2018.02.001
19. Di Carlo T, Khoshnevis B, Carlson A (2013) Experimental and numerical techniques to characterize structural properties of fresh concrete. Mechanics of solids, structures and fluids, Vol 9. San Diego, California, USA, p V009T10A062. American Society of Mechanical Engineers
20. Casagrande L, Esposito L, Menna C, Asprone D, Auricchio F (2020) Effect of testing procedures on buildability properties of 3D-printable concrete. Constr Build Mater 245:118286. https://doi.org/10.1016/j.conbuildmat.2020.118286
21. Wolfs RJM, Bos FP, Salet TAM (2019) Triaxial compression testing on early age concrete for numerical analysis of 3D concrete printing. Cem Concr Compos 104:103344. https://doi.org/10.1016/j.cemconcomp.2019.103344
22. Jayathilakage R, Sanjayan J, Rajeev P (2019) Direct shear test for the assessment of rheological parameters of concrete for 3D printing applications. Mater Struct 52:12. https://doi.org/10.1617/s11527-019-1322-4
23. Le TT, Austin SA, Lim S, Buswell RA, Gibb AGF, Thorpe T (2012) Mix design and fresh properties for high-performance printing concrete. Mater Struct 45:1221–1232. https://doi.org/10.1617/s11527-012-9828-z
24. Panda B, Chandra Paul S, Jen Tan M (2017) Anisotropic mechanical performance of 3D printed fiber reinforced sustainable construction material. Mater Lett 209:146–149. https://doi.org/10.1016/j.matlet.2017.07.123
25. Nerella VN, Hempel S, Mechtcherine V (2019) Effects of layer-interface properties on mechanical performance of concrete elements produced by extrusion-based 3D-printing. Constr Build Mater 205:586–601. https://doi.org/10.1016/j.conbuildmat.2019.01.235
26. Le TT, Austin SA, Lim S, Buswell RA, Law R, Gibb AGF et al (2012) Hardened properties of high-performance printing concrete. Cem Concr Res 42:558–566. https://doi.org/10.1016/j.cemconres.2011.12.003
27. Paul SC, Tay YWD, Panda B, Tan MJ (2018) Fresh and hardened properties of 3D printable cementitious materials for building and construction. Arch Civil Mech Eng 18:311–319. https://doi.org/10.1016/j.acme.2017.02.008
28. Wolfs RJM, Bos FP, Salet TAM (2019) Hardened properties of 3D printed concrete: the influence of process parameters on interlayer adhesion. Cem Concr Res 119:132–140. https://doi.org/10.1016/j.cemconres.2019.02.017
29. Marchment T, Xia M, Dodd E, Sanjayan J, Nematollahi B (2017) Effect of delay time on the mechanical properties of extrusion-based 3D printed concrete. Taipei, Taiwan. https://doi.org/10.22260/ISARC2017/0032
30. van den Heever M, Bester F, Kruger J, van Zijl G (2021) Mechanical characterisation for numerical simulation of extrusion-based 3D concrete printing. J Build Eng 44:102944. https://doi.org/10.1016/j.jobe.2021.102944
31. Feng P, Meng X, Chen J-F, Ye L (2015) Mechanical properties of structures 3D printed with cementitious powders. Constr Build Mater 93:486–497. https://doi.org/10.1016/j.conbuildmat.2015.05.132
32. Sanjayan JG, Nematollahi B, Xia M, Marchment T (2018) Effect of surface moisture on inter-layer strength of 3D printed concrete. Constr Build Mater 172:468–475. https://doi.org/10.1016/j.conbuildmat.2018.03.232
33. Bos F, Menna C, Robens-Radermacher A, Wolfs R, Roussel N, Lombois-Burger H et al (2025) Mechanical properties of 3D printed concrete: a RILEM TC 304-ADC interlaboratory study—approach and main results. Mater Struct 58:183. https://doi.org/10.1617/s11527-025-02686-x
34. Mechtcherine V, Muthukrishnan S, Robens-Radermacher A, Wolfs R, Versteege J, Menna C et al (2025) Mechanical properties of 3D printed concrete: a RILEM 304-ADC interlaboratory study—compressive strength and modulus of elasticity. Mater Struct 58:181. https://doi.org/10.1617/s11527-025-02688-9
35. Wolfs R, Versteege J, Santhanam M, Bhattacherjee S, Bos F, Robens-Radermacher A et al (2025) Mechanical properties of 3D printed concrete: a RILEM TC 304-ADC interlaboratory study—flexural and tensile strength. Mater Struct 58:182. https://doi.org/10.1617/s11527-025-02687-w
36. Panda B, Paul SC, Mohamed NAN, Tay YWD, Tan MJ (2018) Measurement of tensile bond strength of 3D printed geopolymer mortar. Measurement 113:108–116. https://doi.org/10.1016/j.measurement.2017.08.051
37. Napolitano R, Menna C, Asprone D, Del Giudice L (2020) Mechanical characterizatio of layer-by-layer interface in concrete elements obtained by additive manufacturing. In: Bos FP, Lucas SS, Wolfs RJM, Salet TAM (eds) International union of laboratories and experts in construction materials, systems and structures. Second RILEM international conference on concrete and digital fabrication: digital concrete. Cham: Springer
38. EN 1052-3 (2002).Methods of test for masonry—Part 3: Determination of initial shear strength
39. Alchaar AS, Al-Tamimi AK (2021) Mechanical properties of 3D printed concrete in hot temperatures. Constr Build

Mater 266:120991. https://doi.org/10.1016/j.conbuildmat.2020.120991
40. Rahul AV, Santhanam M, Meena H, Ghani Z (2019) Mechanical characterization of 3D printable concrete. Constr Build Mater 227:116710. https://doi.org/10.1016/j.conbuildmat.2019.116710
41. Meurer M, Classen M (2021) Mechanical properties of hardened 3D printed concretes and mortars—development of a consistent experimental characterization strategy. Materials 14:752. https://doi.org/10.3390/ma14040752
42. van den Heever M, du Plessis A, Bester F, Kruger J, van Zijl G (2022) A mechanistic evaluation relating microstructural morphology to a modified Mohr–Griffith compression-shear constitutive model for 3D printed concrete. Constr Build Mater 325:126743. https://doi.org/10.1016/j.conbuildmat.2022.126743
43. ASTM D5607-95 Standard test method for performing laboratory direct shear strength tests of rock specimens under constant normal force
44. Espeche AD, León J (2011) Estimation of bond strength envelopes for old-to-new concrete interfaces based on a cylinder splitting test. Constr Build Mater 25:1222–1235. https://doi.org/10.1016/j.conbuildmat.2010.09.032
45. Giraldo Soto A, Kaufmann W (2021) Effect of test setups on the shear transfer capacity across cracks in FRC. In: Serna P, Llano-Torre A, Martí-Vargas JR, Navarro-Gregori J (eds) Fibre reinforced concrete: improvements and innovations, vol 30. Springer International Publishing, Cham, pp 163–175. https://doi.org/10.1007/978-3-030-58482-5_15
46. Zanotti C, Randl N (2019) Are concrete-concrete bond tests comparable? Cem Concr Compos 99:80–88. https://doi.org/10.1016/j.cemconcomp.2019.02.012
47. Licciardello L, Soto AG, Kaufmann W, Metelli G (2025) Determining the strength of 3D printed concrete with the modified slant shear test. Struct Concr 26:2467–2486. https://doi.org/10.1002/suco.202400238
48. Kinomura K, Murata S, Yamamoto Y, Obi H, Hata A (2020) Application of 3D printed segments designed by topology optimization analysis to a practical scale prestressed pedestrian bridge. In: Bos FP, Lucas SS, Wolfs RJM, Salet TAM (eds) Second RILEM international conference on concrete and digital fabrication, vol 28. Springer International Publishing, Cham, pp 658–668. https://doi.org/10.1007/978-3-030-49916-7_66
49. Gebhard L, Bischof P, Anton A, Mata-Falcón J, Dillenburger B, Kaufmann W (2022) Pre-installed reinforcement for 3D concrete printing. In: Buswell R, Blanco A, Cavalaro S, Kinnell P (eds) Third RILEM international conference on concrete and digital fabrication, vol 37. Springer International Publishing, Cham, pp 430–435. https://doi.org/10.1007/978-3-031-06116-5_64
50. Asprone D, Auricchio F, Menna C, Mercuri V (2018) 3D printing of reinforced concrete elements: technology and design approach. Constr Build Mater 165:218–231. https://doi.org/10.1016/j.conbuildmat.2018.01.018
51. Van Der Putten J, Van Olmen A, Aerts M, Ascione E, Beneens J, Blaakmeer J et al (2020) 3D Concrete printing on site: a novel way of building houses? In: Bos FP, Lucas SS, Wolfs RJM, Salet TAM (eds) Second RILEM international conference on concrete and digital fabrication, vol 28. Springer International Publishing, Cham, pp 712–719. https://doi.org/10.1007/978-3-030-49916-7_71
52. Bos F, Wolfs R, Ahmed Z, Salet T (2019) Large scale testing of digitally fabricated concrete (DFC) elements. In: Wangler T, Flatt RJ (eds) First RILEM international conference on concrete and digital fabrication—digital concrete 2018, vol 19. Springer International Publishing, Cham, pp 129–147. https://doi.org/10.1007/978-3-319-99519-9_12
53. Bos FP, Menna C, Pradena M, Kreiger E, da Silva WRL, Rehman AU et al (2022) The realities of additively manufactured concrete structures in practice. Cem Concr Res 156:106746. https://doi.org/10.1016/j.cemconres.2022.106746
54. Mechtcherine V, Van Tittelboom K, Kazemian A, Kreiger E, Nematollahi B, Nerella VN et al (2022) A roadmap for quality control of hardening and hardened printed concrete. Cem Concr Res 157:106800. https://doi.org/10.1016/j.cemconres.2022.106800
55. Bos F, Wolfs R, Ahmed Z, Salet T (2016) Additive manufacturing of concrete in construction: potentials and challenges of 3D concrete printing. Virtual Phys Prototyp 11:209–225. https://doi.org/10.1080/17452759.2016.1209867
56. EN 1015-11 (2019). Method of test for mortar for masonry—Part 11: Determination of flexural strength of hardened mortar
57. EN 12390-13 (2013). Testing hardened concrete. Part 13: Determination of secant modulus of elasticity in compression
58. Licciardello L, Reggia A, Metelli G, Plizzari G (2021) Investigation of the interlayer strength of 3D printed concrete shear walls. 14th fib PhD symposium in Civil Engineering, Rome
59. European Committee for Standardisation. EN 1992-2: Eurocode 2: design of concrete structures—Part 2: concrete bridges–design and detailing rules. 2005
60. Ferretti F, Mazzotti C, Esposito R, Rots JG (2018) Shear-sliding behavior of masonry: Numerical micro-modeling of triplet tests. Computational modelling of concrete structures. 1st ed., CRC Press, London, pp 941–951. https://doi.org/10.1201/9781315182964-109
61. Bompa DV, Elghazouli AY (2020) Experimental and numerical assessment of the shear behaviour of lime mortar clay brick masonry triplets. Constr Build Mater 262:120571. https://doi.org/10.1016/j.conbuildmat.2020.120571
62. van den Heever M, Bester F, Kruger J, van Zijl G (2022) Numerical modelling strategies for reinforced 3D concrete printed elements. Addit Manuf 50:102569. https://doi.org/10.1016/j.addma.2021.102569
63. DIANA FEA. https://dianafea.com/
64. Lourenço PB, Rots JG (1997) Multisurface interface model for analysis of masonry structures. J Eng Mech 123:660–668. https://doi.org/10.1061/(ASCE)0733-9399(1997)123:7(660)
65. Manuals for DIANA FEA. https://manuals.dianafea.com
66. Comité euro-international du béton, editor. (2013) Fib model code for concrete structures 2010. Ernst & Sohn, Berlin

67. Feenstra PH (1993) Computational aspects of biaxial stress in plain and reinforced concrete
68. Rots JG (1988) Computational Modeling of Concrete Fracture
69. Lourenco PB (1996) A user/programmer guide for the micro-modelling of masonry structures